


Article

Gust Modeling with State-of-the-Art Computational Fluid Dynamics (CFD) Software and Its Influence on the Aerodynamic Characteristics of an Unmanned Aerial Vehicle

Michał Frant ¹, Stanisław Kachel ¹ and Wojciech Maślanka ^{2,*}

¹ Faculty of Mechatronics, Armament and Aerospace, Military University of Technology, No. 2 Kaliskiego Street, 00-908 Warsaw, Poland; michal.frant@wat.edu.pl (M.F.); stanislaw.kachel@wat.edu.pl (S.K.)

² Doctoral School, Military University of Technology, No. 2 Kaliskiego Street, 00-908 Warsaw, Poland

* Correspondence: wojciech.maslanka@wat.edu.pl; Tel.: +48-501-312-587

Abstract: The aim of this article is to propose methods for obtaining the aerodynamic characteristics of a flying object in a turbulent atmosphere. This article presents static aerodynamic characteristics of an unmanned aerial vehicle (UAV), which have been obtained during experimental examinations and during numerical calculations. The results have been compared with each other in order to validate the numerical model and methods. The method for modeling gusts using state-of-the-art CFD software (i.e., ANSYS Fluent Release 16.2) has been proposed and applied to obtain the aerodynamic characteristics of a UAV including during gusts. Two cases have been analyzed. In the first case, a downburst was modeled. In the second case, a single oblique gust was modeled (i.e., changing the angle of attack and the angle of sideslip), that had a complicated time course in regard to its velocity. Although this article is focused on the assessment of the vulnerability of a UAV model to gusts, the practical implications of the proposed methodology are applicable to a wide selection of objects, including wind turbines.

Keywords: aerodynamics; computational fluid dynamics; unmanned aerial vehicle; gusts



Citation: Frant, M.; Kachel, S.; Maślanka, W. Gust Modeling with State-of-the-Art Computational Fluid Dynamics (CFD) Software and Its Influence on the Aerodynamic Characteristics of an Unmanned Aerial Vehicle. *Energies* **2023**, *16*, 6847. <https://doi.org/10.3390/en16196847>

Academic Editor: Andrey A. Kurkin

Received: 26 August 2023

Revised: 14 September 2023

Accepted: 26 September 2023

Published: 27 September 2023



Copyright: © 2023 by the authors. Licensee MDPI, Basel, Switzerland. This article is an open access article distributed under the terms and conditions of the Creative Commons Attribution (CC BY) license (<https://creativecommons.org/licenses/by/4.0/>).

1. Introduction

Gusts are considered to be one of the most dangerous weather phenomena for aircraft. There are plenty of publications characterizing wind gusts, in which data have been obtained during experimental research using different techniques [1–5], as well as during numerical calculations [6]. They show that some gusts have a velocity exceeding 20 m/s, while the time to reach its maximum speed is less than 1 s. Such severe conditions could even cause the crash of a large airliner [7], whereas small and slow flying objects like general aviation aircraft, unmanned aerial vehicles (UAVs) or paragliders are incomparably more sensitive to a turbulent atmosphere [8,9]. Thus, studies on UAVs flight control methods in a gusty environment seem to be of great importance. Such research was conducted by Chodnicki M. et al. [10].

It should be noted that gusts may also be hazardous for wind turbines. Therefore, this subject area is also identified as particularly significant and present in numerous studies [11–13].

The influence of gusts on the aerodynamic characteristics of a flying object is problematic to examine experimentally. As presented by Yitao Z. et al. [14] and by Reischich A. et al. [15], it requires the installation of additional devices in a wind tunnel to change the airflow direction in proximity to the tested object. Concurrently, numerical methods, i.e., computational fluid dynamics (CFD), seem to be more convenient for the examination of transient flows, including modelling gusts. Kotsiopoulou M. and Bouris D. conducted and described the numerical simulation of a single gust on the flow past a two-dimensional body [16], while Lakshmi S. et al., examined the effect of a macroscopic turbulent gust on the aerodynamic

performance of a vertical axis wind turbine in a 3D space [17]. In this case, the time-dependent velocity course was introduced on the boundaries of the computational domain to simulate the gust. It should be noted that CFD software seems to be the most appropriate tool for obtaining aerodynamic loads on wind turbine blades, which can be utilized for structural tests. Such combined analysis has been conducted by Santo G. et al. [18], as well as by Cai X. et al. [19].

State-of-the-art CFD software (ANSYS Fluent Release 16.2, Canonsburg, PA, USA) allows calculations to be conducted for transient cases, real size objects, as well as for the full range of flight velocities. Moreover, because of easiness of modifying virtual models, it seems to be an appropriate tool for aerodynamic shape optimization problems, as indicated by Benaouali A. and Kachel S. [20]. However, the obtained results might vary depending on the calculation domain geometry, boundary condition, finite volume mesh, and physical and numerical models, etc. Therefore, the calculated results should be compared with measurements conducted experimentally (for instance in a wind tunnel) to validate the CFD models. Depending on the specific case, this comparison may be related to the qualitative aspects of airflow (for example, the investigation of streamlines or particle tracks around the physical and virtual model as presented by Kozakiewicz A. et al. [21]), flow quantities like the aerodynamic coefficients or pressure field [22], or both aspects mentioned above. Comprehensive experimental and numerical studies on the aerodynamic characteristics of UAVs have been described by Frant M. [23]. It should be noted that more strategic approaches to aerodynamic studies include uncertainty quantification (UQ) analysis [24–26].

Let us notice that there is variety of publications on UAVs aerodynamics, which includes numerical analysis [27], as well as combined experimental and CFD investigation [28,29]. The purposes of the identified works are mostly aerodynamic shape optimization [30] or examination of the influence of flight conditions on the aerodynamic characteristics of UAVs [31,32], which is also a topic of the presented work. However, in the analyzed studies, the influence of gusts dynamically changing the flow velocity magnitude and angles has not been assessed, which is considered as a novelty of the presented study.

Considering the above, the following tests were performed to obtain the aerodynamic characteristics of a UAV in a turbulent atmosphere:

- First, the steady-state aerodynamic characteristics were determined experimentally using a wind tunnel and numerically using ANSYS Fluent Release 16.2 software. The experimental results allowed the numerical model to be validated;
- After obtaining a satisfactory convergence in the results, numerical calculations analyzing the impact of gusts on the aerodynamic characteristics of a UAV were performed. Time-dependent boundary conditions determined with the so-called user-defined functions (UDFs) were proposed to simulate the gust.

The aim of this article was to discuss in detail the proposed research methodology and the obtained results, as well as to demonstrate the potential for solving complex non-stationary airflow problems using the ANSYS Fluent Release 16.2 package.

2. Materials and Methods

2.1. Model under Examination

The subject of the presented study was a 1:5 scale model of the reconnaissance UAV Rybitwa, which was designed at the Military University of Technology (MUT). Figure 1 presents the geometry of the model in three views, with the main geometrical data superimposed. The aerodynamic configuration of the UAV under investigation includes a straight wing (with wingtips directed upwards for increased lateral stability) and T-tail assembly. The payload pod is hung under the fuselage, such arrangement allows to the UAV to be easily equipped with proper reconnaissance instruments for a given mission.

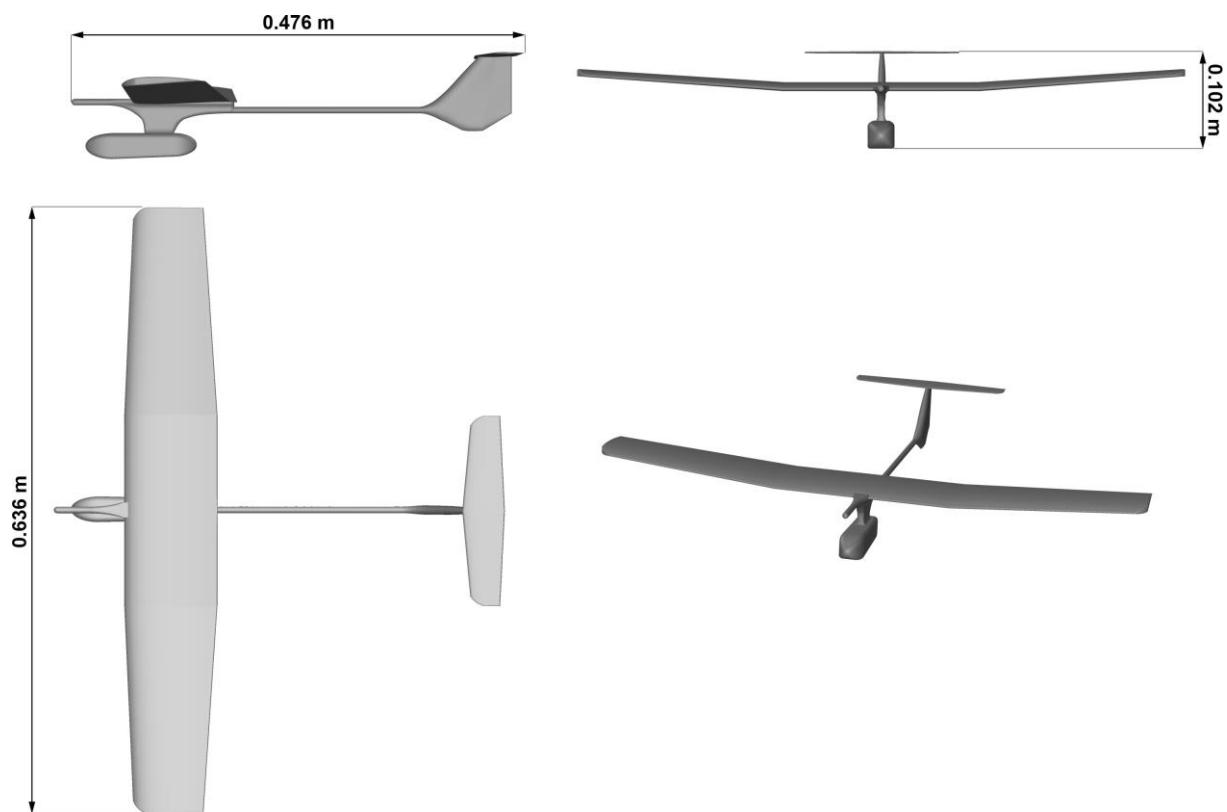


Figure 1. UAV under examination.

It should be noted that the gross wing area and mean aerodynamic chord of the UAV under examination (accordingly 0.0571 m^2 and 0.09 m) were used as the reference area and length during the experimental and numerical investigations.

2.2. Measurement System for Experimental Investigation

An experimental investigation was conducted in a low-speed wind tunnel at the Military University of Technology (MUT), Warsaw. The maximal velocity of the airflow in the measuring space is around 60 m/s and the diameter of the test section is equal to 1.1 m .

Figure 2 shows a schematic of the measurement system used during the experimental investigation. The main instrument in this system is a closed-return wind tunnel. It should be noted that the tunnel is equipped with an installation to simulate icy conditions. Although the installation was not used in the present study, let us notice that the experimental icy simulation capabilities at MUT are unique across Poland.

Figure 3 presents the test section of the wind tunnel, as well as the attachment of the UAV model to an aerodynamic balance. As presented, the aerodynamic balance in the MUT low-speed wind tunnel has an annular shape. The models under investigation are attached to it with strings with known drag.

The aerodynamic balance can be supported in order to rotate freely about the A-A, B-B or C-C axis. Aerodynamic forces and moments acting on the models under examination produce torques about the abovementioned axes. Thus, the measurement of the forces acting on a lever in the aerodynamic balance allows the aerodynamic forces and moments to be determined.

It should be noted that depending on the applied support option (A-A, B-B or C-C), there is the possibility to measure only one aerodynamic force (or moment of force) at once.

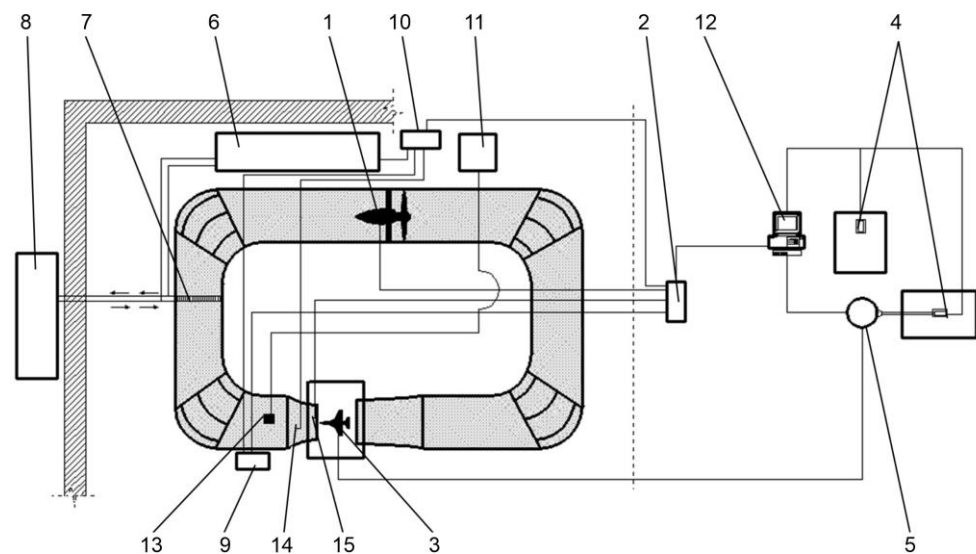


Figure 2. Schematic of the measurement system. 1: fan, 2: inverter, 3: model under examination, 4: strain gauges (0.01 N accuracy), 5: aerodynamic balance, 6: compressors in the cooling system, 7: cooler unit, 8: condenser, 9: control panel, 10: control cabinet for the compressors, 11: water compressor, 12: data acquisition and measurement control subsystem, 13: water injectors, 14: humidity sensor and 15: Prandtl tube (1 Pa accuracy).

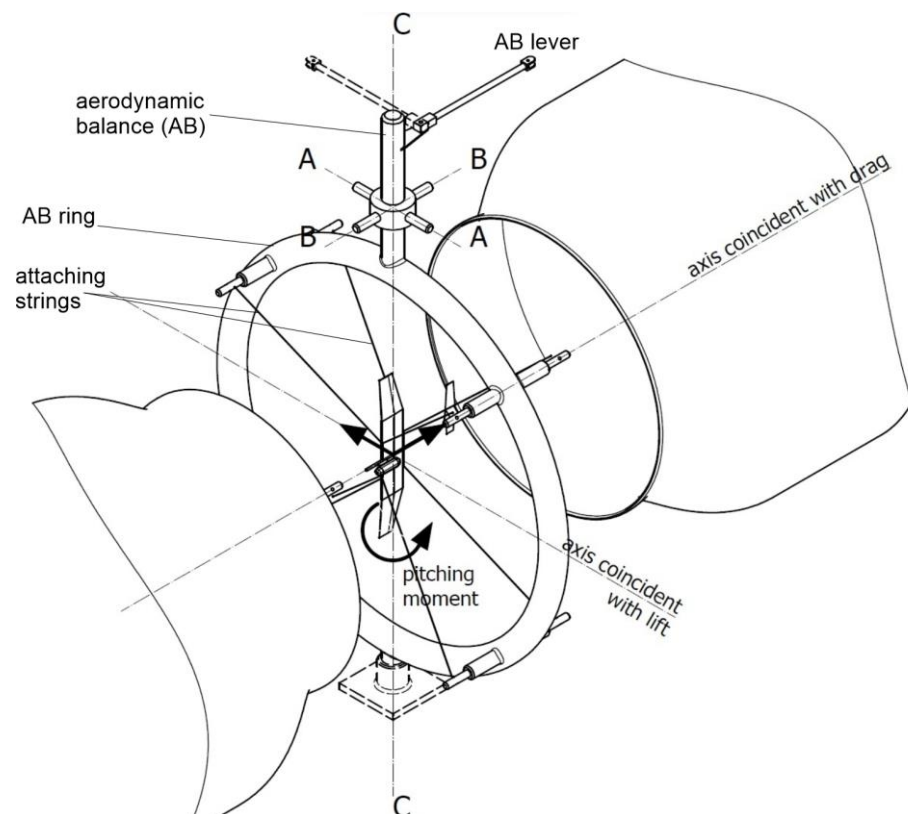


Figure 3. Attachment of the UAV model to the aerodynamic balance.

Regardless of the applied support option, a ring in the aerodynamic balance (with the model attached) may be rotated about the C-C axis to obtain a different position for the model under examination. The rotation is executed by a separate mechanism based on a warm drive.

Figure 4 shows the UAV model during the tests in the wind tunnel. The attachment of the model was that its longitudinal axis coincided with the longitudinal axis of the tunnel (when the angle of attack equaled zero), while its transverse axis coincided with the tunnel's vertical axis, as shown in Figure 3. The attachment allowed the values on the lift force, drag force or pitching moment for different angles of attack to be obtained.

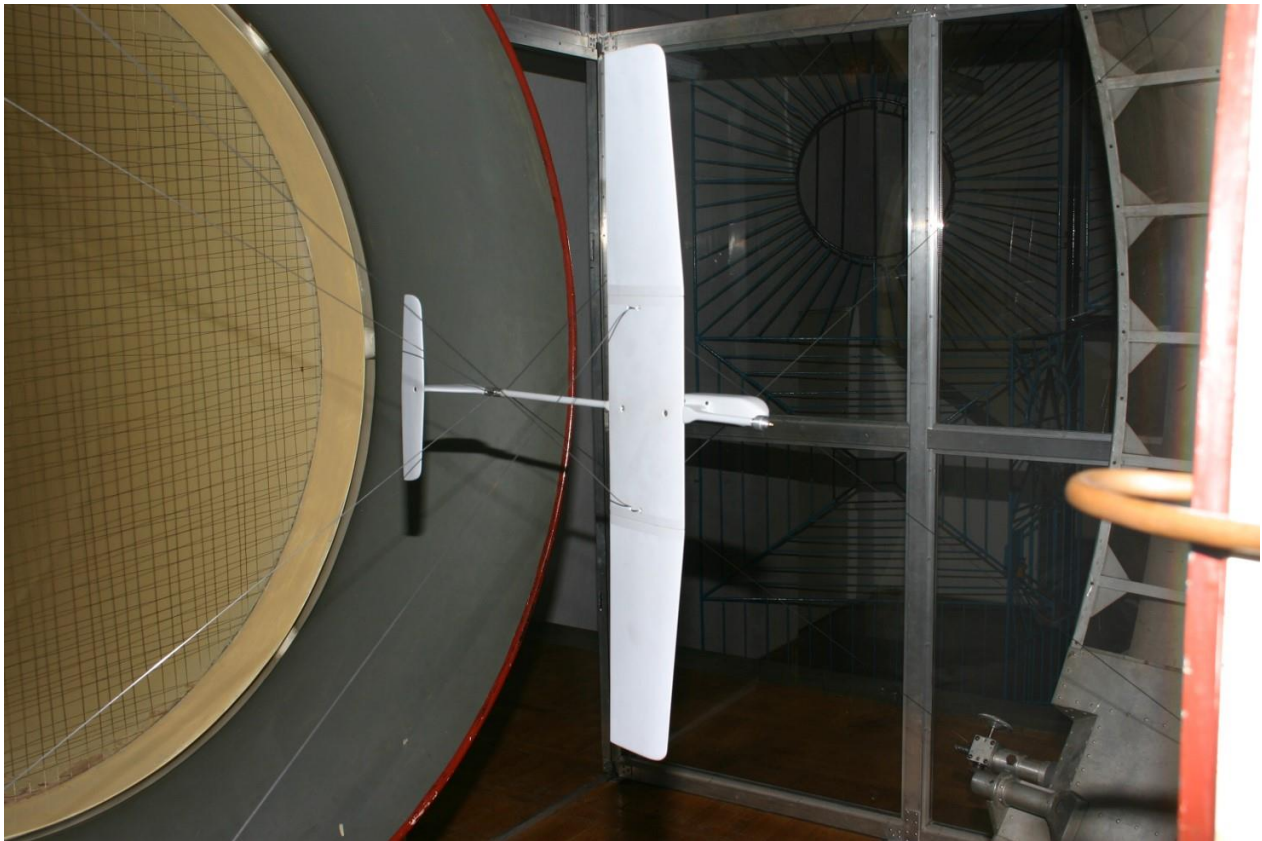


Figure 4. UAV model during tests in the wind tunnel.

The aerodynamic forces and pitching moments obtained in the wind tunnel were utilized to calculate the values of the aerodynamic coefficients, which were used for the validation of the numerical model.

2.3. CFD Calculations

The calculations were conducted in ANSYS Fluent Release 16.2. The steady state, as well as transient cases were analyzed. The aim of the steady-state calculations was the evaluation of the mesh quality, as well as the choice of the most adequate turbulence model for the considered case. The main focus of the study was transient simulations conducted to assess the gust influence on the UAV's aerodynamic characteristics.

2.3.1. Governing Equations

ANSYS Fluent Release 16.2 is based on a finite volume method. For a realizable $k-\varepsilon$ turbulence model, which showed the most adequate results, the solver utilizes Reynolds Averaged Navier–Stokes (RANS) equations. They can be written in Cartesian tensor form [33]:

$$\begin{aligned} \frac{\partial \rho}{\partial t} + \frac{\partial}{\partial x_i}(\rho u_i) &= 0 \\ \frac{\partial}{\partial t}(\rho u_i) + \frac{\partial}{\partial x_j}(\rho u_i u_j) &= -\frac{\partial p}{\partial x_i} + \frac{\partial}{\partial x_j} \left[\mu \left(\frac{\partial u_i}{\partial x_j} + \frac{\partial u_j}{\partial x_i} - \frac{2}{3} \delta_{ij} \frac{\partial u_l}{\partial x_l} \right) \right] + \frac{\partial}{\partial x_j}(\rho \overline{u_i' u_j'}) \end{aligned} \quad (1)$$

The term $\overline{\rho u_i' u_j'}$ represents the so-called Reynolds stresses, which have to be modeled to close the RANS equations. The family of k - ε turbulence models is based on transport equations for the kinetic energy (k) and its dissipation rate (ε). The governing equations for k and ε for a realizable k - ε model are as follows [33]:

$$\begin{aligned} \frac{\partial}{\partial t}(\rho k) + \frac{\partial}{\partial x_j}(\rho k u_j) &= \frac{\partial}{\partial x_j} \left[\left(\mu + \frac{\mu_T}{\sigma_k} \right) \frac{\partial k}{\partial x_j} \right] + G_k + G_b + \rho \varepsilon - Y_M + S_k \\ \frac{\partial}{\partial t}(\rho \varepsilon) + \frac{\partial}{\partial x_j}(\rho \varepsilon u_j) &= \frac{\partial}{\partial x_j} \left[\left(\mu + \frac{\mu_T}{\sigma_\varepsilon} \right) \frac{\partial \varepsilon}{\partial x_j} \right] + \rho C_1 S \varepsilon - \rho C_2 \frac{\varepsilon^2}{k + \sqrt{\nu \varepsilon}} + C_{1\varepsilon} \frac{\varepsilon}{k} C_{3\varepsilon} G_b + S_\varepsilon \end{aligned} \quad (2)$$

In the above equations, G_k and G_b represent the generation of turbulent kinetic energy due to the mean velocity gradients and buoyancy, accordingly. Y_M represents the contribution of the fluctuating dilatation in the compressible turbulence to the overall dissipation rate, while S_k and S_ε are user-defined source terms. The relationship between k , ε and turbulent viscosity is presented below [33]:

$$\pi_t = \rho C_\mu \frac{k^2}{\varepsilon} \quad (3)$$

The default values for constants C_1 , C_2 , $C_{1\varepsilon}$, $C_{3\varepsilon}$, C_μ , σ_k and σ_ε were left in accordance with the ANSYS Fluent Release 16.2 selection.

2.3.2. Numerical Model

During the numerical calculations, the hybrid finite volume mesh was utilized, which consisted of tetrahedral elements in the majority of the calculation domain, as well as prisms in the boundary layer region (the boundary layer included 5 prismatic layers with the wall $y+$ value below 1 on most of the UAV surfaces). The total element count was 2,069,466 cells. The obtained minimum and maximum cell volumes were $9.4 \times 10^{-14} \text{ m}^3$ and 0.43 m^3 , accordingly.

The calculation domain had the shape of a cuboid, which extended from -3.7 m to 8.6 m along the OX axis, and from -4.3 m to 4.3 m along the OY and OZ axes. The UAV model under examination was subtracted from the cuboid. The types of applied boundary conditions are shown in Table 1 below.

Table 1. Applied boundary conditions.

Location	Name	Type
outer surfaces	outer	pressure far-field
fuselage of UAV	fuselage	wall
wings of UAV	wing	wall
horizontal stabilizer of UAV	horizontal_stab	wall
vertical stabilizer of UAV	vert_stab	wall

The pressure-based solver with the SIMPLE calculation algorithm was utilized. The second-order discretization schemes were set, which was a trade-off between accuracy and stability during calculations for transient cases.

It should be noted that the mesh sensitivity tests were performed during another study [23]. Six hybrid meshes with different element counts (from 1,895,971 to 5,163,438), heights of the first prismatic layer (from $1.3 \times 10^{-5} \text{ m}$ to $5 \times 10^{-4} \text{ m}$) and number of prism layers (from 5 to 10) were tested. The mesh used in the present study proved to have good accuracy, stability and efficiency. Figure 5 presents the final refinement of the cells on the surfaces of the UAV model, as well as the mesh edges on OXZ plane.

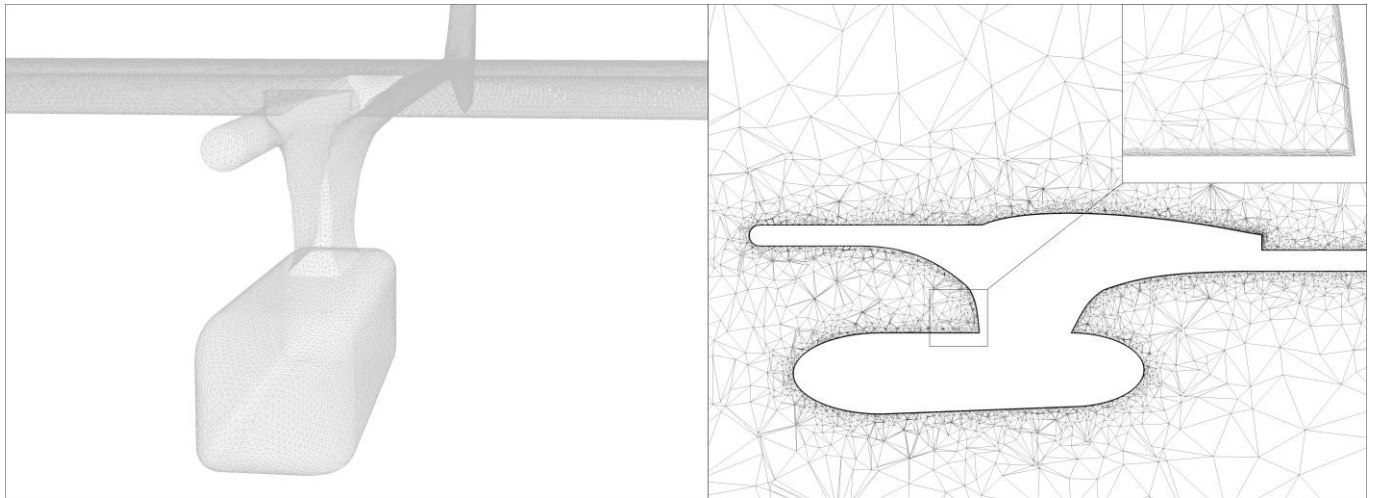


Figure 5. Finite volume mesh.

2.3.3. Gust Modeling Method

A gust acting on a flying object in the atmosphere causes rapid and temporary changes in the airflow velocity vector. Consequently, the speed, angle of attack (α) and angle of sideslip (β) vary in time. In numerical calculations, these parameters are determined on the outer surfaces of the calculation domain. For the pressure far-field boundary condition (which was applied in the analyzed case), the flow velocity vector is defined by the following:

- Mach number;
- X-component of the flow direction;
- Y-component of flow direction;
- Z-component of flow direction.

It should be noted that during numerical calculations relevant to flying objects the axes are usually assumed as follows:

- The OX axis coincides with the longitudinal axis of the studied object and is directed towards its rear;
- The OY axis coincides with the transverse axis and is directed towards the right wing;
- The OZ axis is perpendicular to the OXY plane and directed upwards;
- In the case under analysis, the coordinate system origin was assumed to be at the UAV's center of gravity.

In other words, the axes described above coincide with the body frame axes $Ox_B y_B z_B$, but the X and Z axes have opposite directions in comparison to x_B and z_B , which is convenient when considering the effect of the airflow around a stationary object.

Accordingly, the x_A and z_A axes of the aerodynamic frame are frequently inverted in CFD studies. Such an approach allows the reading of the numerical results to be simplified and clarified. It was also implemented in the present study:

- The Ox_A axis was directed correspondingly in the direction of the air streams and parallel to them;
- The Oz_A axis was directed upwards, perpendicular to the axis Ox_A and lay in the symmetry plane of the model;
- The Oy_A axis was directed to the right and perpendicular to the Ox_A and Oz_A axes.

Modeling a gust in ANSYS Fluent Release 16.2 requires an appropriate determination of the Mach number, as well as the X-, Y-, and Z-components of the flow direction (variable in time) and their assignment to the outer boundary surfaces. Figure 6 shows and describes the gust modeling algorithm used in the calculations.

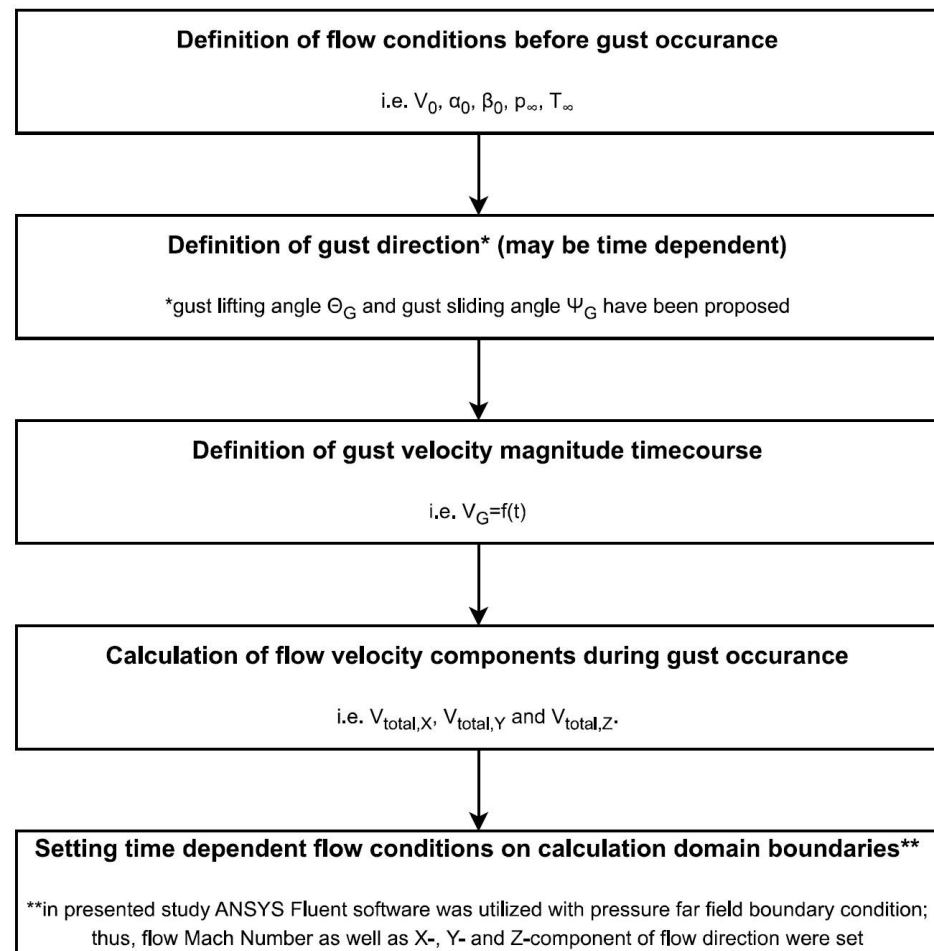


Figure 6. Proposed method for modeling a gust in CFD simulations.

The initial flow conditions (before gust occurrence) were assumed as follows: flow velocity V_0 , angle of attack α_0 and angle of sideslip β_0 . The initial air temperature and pressure were T_∞ and p_∞ , accordingly.

During the numerical calculations, the gust vector \vec{V}_G was defined by the gust velocity magnitude, as well as by two angles, presented in Figure 7. It was proposed to mark them as the gust lifting angle Θ_G and the gust slipping angle Ψ_G . The gust lifting angle Θ_G was assumed to be the angle between the Ox_A axis and the projection of the gust velocity vector \vec{V}_G onto the Ox_Az_A plane. Angle Θ_G was assumed to be positive when the angle of attack increased. The gust slipping angle Ψ_G was the angle between the Ox_A axis and the projection of the gust velocity vector onto the Ox_Ay_A plane. As the positive angle Ψ_G , it was considered to be the one increasing the angle of the sideslip.

An exemplary course of the gust velocity magnitude is shown in Figure 8. In this course, the velocity increases sinusoidally to the maximum value, then remains at a constant level for some time, and finally decreases sinusoidally to zero. In this case, the function $V_G = f(t)$ is in the form:

$$\begin{cases} V_G = 0, & \text{for } t < T_0 \\ V_G = 0.5 \times V_{G,MAX} \times \left[1 - \cos\left(\pi \times \frac{t-T_0}{T_1}\right) \right], & \text{for } T_0 \leq t < T_0 + T_1 \\ V_G = V_{G,MAX}, & \text{for } T_0 + T_1 \leq t < T_0 + T_1 + T_2 \\ V_G = 0.5 \times V_{G,MAX} \times \left[1 + \cos\left(\pi \times \frac{t-T_0-T_1-T_2}{T_3}\right) \right], & \text{for } T_0 + T_1 + T_2 \leq t < T_0 + T_1 + T_2 + T_3 \\ V_G = 0, & \text{for } t \geq T_0 + T_1 + T_2 + T_3 \end{cases} \quad (4)$$

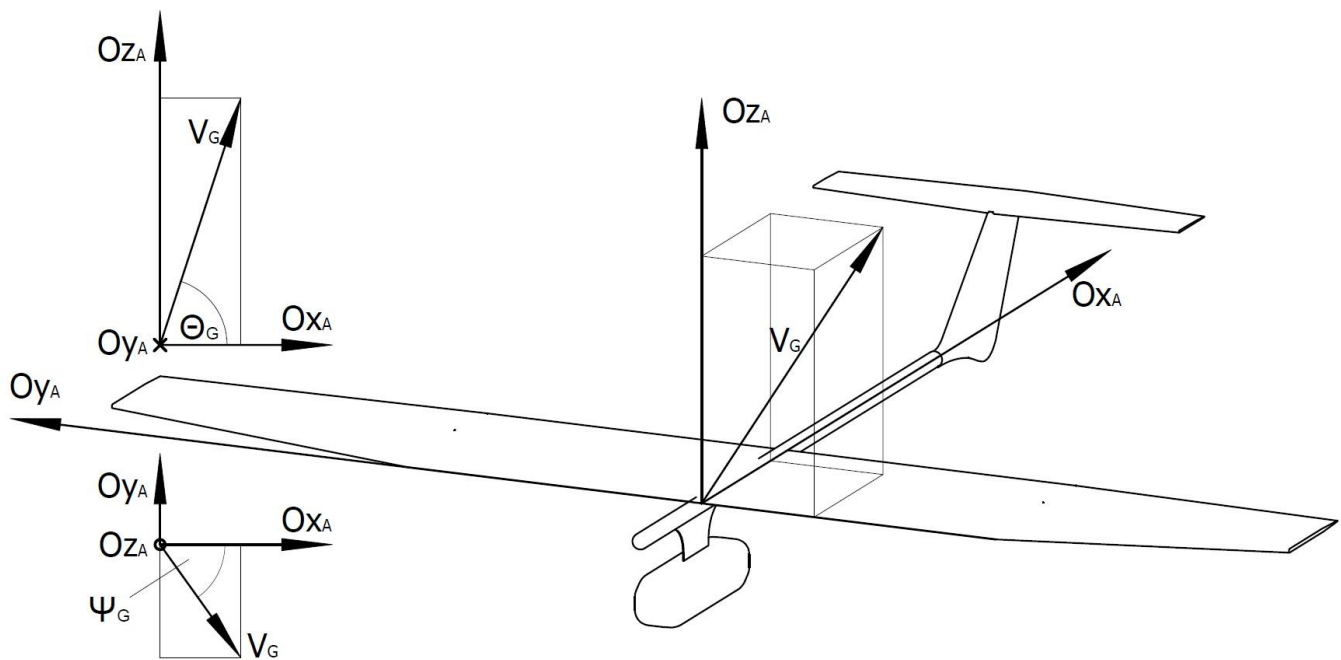


Figure 7. Explanation of gust lifting and slipping angles in the present study.

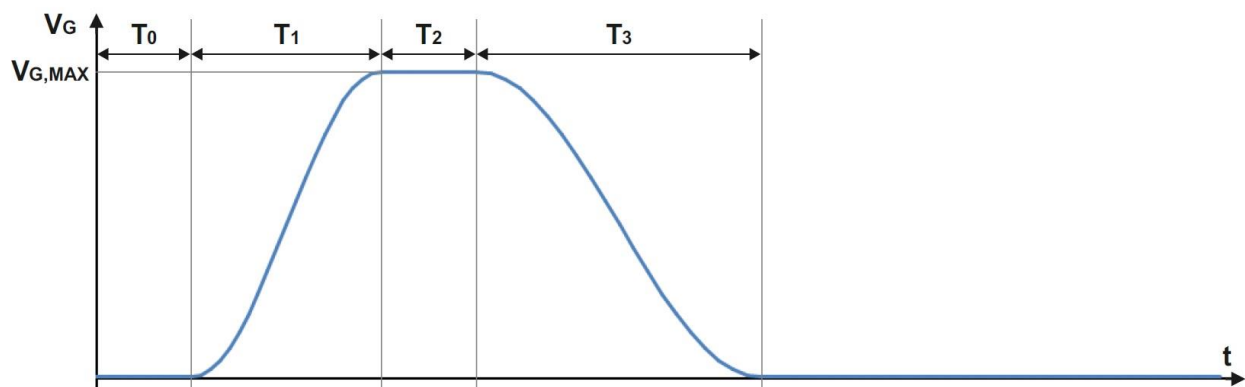


Figure 8. Exemplary time course of the gust velocity magnitude.

In the considered case, in order to characterize the gust, values should be assigned to the maximum gust velocity $V_{G,MAX}$ and the time intervals T_0 , T_1 , T_2 and T_3 .

The calculation of the flow velocity components, with the gust consideration, was conducted in three stages, described below.

First, the \vec{V}_G vector was projected into the components acting along the axis of the $Ox_Ay_Az_A$ ($t = 0$) system. The following transformations were applied:

$$\begin{aligned}
 V_{G,xA0} &= V_G \times \cos \Theta_G \times \cos \Psi_G \\
 V_{G,yA0} &= V_G \times \cos \Theta_G \times \sin \Psi_G \\
 V_{G,zA0} &= V_G \times \sin \Theta_G
 \end{aligned}
 \tag{5}$$

The next step was to determine the total flow velocity \vec{V}_{total} , which was composed of the initial flow velocity \vec{V}_0 and the gust velocity \vec{V}_G . The components of the \vec{V}_{total} in the $Ox_Ay_Az_A$ ($t = 0$) system were described by the following formulas:

$$\begin{aligned} V_{total,xA0} &= V_0 + V_{G,xA0} \\ V_{total,yA0} &= -V_{G,yA0} \\ V_{total,zA0} &= V_{G,zA0} \end{aligned} \quad (6)$$

The minus sign in the expression for $V_{total,yA0}$ resulted from the assumption that the positive gust slipping angle increased the angle of the sideslip. Thus, a gust with a positive Ψ_G had a velocity component directed from the right wing towards the left wing. This was in the direction of $-Oy_A$ in the adopted coordinate system.

The last step was to transform the components of the vector \vec{V}_{total} into the system OXYZ associated with the computational mesh. A suitable transformation matrix was utilized [34], which was modified accordingly because of the assumed axis directions:

$$\begin{aligned} V_{total,X} &= \cos \alpha_0 \times \cos \beta_0 \times V_{total,xA0} + \cos \alpha_0 \times \sin \beta_0 \times V_{total,yA0} - \sin \alpha_0 \times V_{total,zA0} \\ V_{total,Y} &= -\sin \beta_0 \times V_{total,xA0} + \cos \beta_0 \times V_{total,yA0} \\ V_{total,Z} &= \sin \alpha_0 \times \cos \beta_0 \times V_{total,xA0} + \sin \alpha_0 \times \sin \beta_0 \times V_{total,yA0} + \cos \alpha_0 \times V_{total,zA0} \end{aligned} \quad (7)$$

Based on the values of $V_{total,X}$, $V_{total,Y}$ and $V_{total,Z}$, the following expression could be used to determine the Mach number and the X-, Y- and Z-components of flow direction:

$$\begin{aligned} \text{Mach Number} &= \frac{\sqrt{V_{total,X}^2 + V_{total,Y}^2 + V_{total,Z}^2}}{\sqrt{\gamma \times R \times T_\infty}} \\ \text{X - Component of Flow Direction} &= \frac{V_{total,X}}{\sqrt{V_{total,X}^2 + V_{total,Y}^2 + V_{total,Z}^2}} \\ \text{Y - Component of Flow Direction} &= \frac{V_{cY}}{\sqrt{V_{total,X}^2 + V_{total,Y}^2 + V_{total,Z}^2}} \\ \text{Z - Component of Flow Direction} &= \frac{V_{c,Z}}{\sqrt{V_{total,X}^2 + V_{total,Y}^2 + V_{total,Z}^2}} \end{aligned} \quad (8)$$

In the formulas above, γ describes the adiabatic index, and R describes the individual gas constant of air.

The flow parameters, calculated according to the formulas above, could be inserted on the outer surfaces of the calculation area. However, it was not possible to define the boundary conditions that change over time using the standard menu in ANSYS Fluent Release 16.2. This could be accomplished by utilizing the so-called UDFs (user-defined functions). The UDFs are functions written in the C programming language by the Fluent user, which allows the standard features of this software to be enhanced. In the present study, UDFs were utilized to determine the time-varying flow parameters on the boundary surfaces of the calculation area.

Let us notice that the manual [35] contains descriptions of the functions and commands used in UDFs and examples of their use.

3. Results and Discussion

3.1. Numerical Models Validation

Experimental studies were carried out for the Mach and Reynolds numbers, where $Ma = 0.12$, $Re = 2.74 \times 10^5$ (which corresponds to the speed of the air equal to 42 m/s). The applied angles of attack were in the range of $\alpha = -12^\circ \div +12^\circ$, with a 1° step.

A comparison of the characteristics obtained during the experimental and numerical analysis is presented in Figure 9 below.

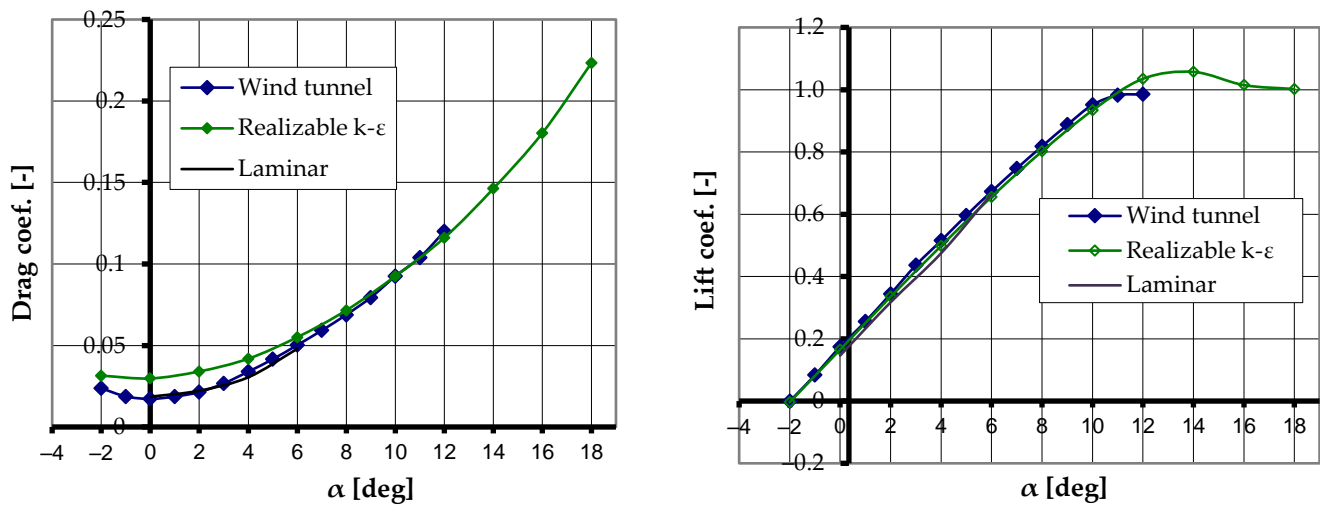


Figure 9. Drag and lift coef. for different angles of attack obtained through experimental and numerical analysis.

As may be read from the above figures, the most approximate to the experimental results were the characteristics obtained with the realizable k- ϵ turbulence model (when $\alpha > 6^\circ$). However, when the angle of attack was in the range of $0^\circ \div 6^\circ$, the most appropriate was laminar model. It should be noted that for moderate angle of attack values, the UAV model may be considered as a streamlined body, whereas for higher values it performs more like bulk geometry. The values of the critical Reynolds number depend on the specific case, for example they may differ significantly when external or internal flows are under examination. Some estimations of the critical Re value for external airflow over a streamlined body may be for a flow over a smooth flat plate, for which $Re_{\text{critical}} = 5 \times 10^5$ is a well-established value [36]. Thus, the assumption of laminar flow for $\alpha \leq 6^\circ$, as well as the presented results, are justified.

Let us note that the impact of gusts on a flying object in the atmosphere may cause short-term fluctuations between large positive and large negative angles of attack. In such conditions, the assumption of flow laminarity is not justified. The aim of this study was to analyze the UAV's aerodynamic characteristics under the influence of gusts. Therefore, the realizable k- ϵ turbulence model was applied in further steps during this research.

3.2. Influence of Gusts on Aerodynamic Characteristics of UAV

In the presented study on the impact of gusts on the aerodynamic characteristics of a UAV, two isolated gusts were modeled. These gusts differed in direction (i.e., gust lifting angle and gust slipping angle), as well as in the time course of the velocity magnitude. The first case involved a simple down draft. In the second case, the impact of an oblique gust (simultaneously changing the angle of attack and the angle of sideslip) on the UAV was studied.

In both cases, the initial velocity equaled $V_0 = 20.84$ m/s, the initial angle of attack and angle of sideslip were assumed to be $\alpha_0 = 2^\circ$ and $\beta_0 = 0^\circ$. The temperature and pressure of the undisturbed stream were $T_\infty = 300$ K and $p_\infty = 101,325$ Pa.

The time step was set at $\Delta t = 0.001$ s. Because the residuals obtained for the steady-state flow were slightly below 0.001 for continuity and below 1×10^{-4} for the remaining equations, the convergence criterion for transient cases was set to 0.001 for all of the residuals. For each time step, the following data were recorded:

- Forces in the OXYZ coordinate system;

- Rolling, pitching and yawing moments (aerodynamic moments were determined relative to the point lying on the leading edge of the wing, in the UAV's symmetry plane);
- Contours of static pressure on the UAV's surfaces.

Based on the forces and moments listed above, the aerodynamic coefficients were calculated (instantaneous values on the velocity, angle of attack and angle of sideslip were utilized). The wing area, which equaled 0.05709 m^2 , was considered to be the reference area and the reference length was identified with the mean aerodynamic chord (0.09 m).

3.2.1. Down Draft

The first gust under study was the down draft (i.e., the gust lifting angle was $\Theta_G = -90^\circ$ and the gust sliding angle was equal to zero). The general form of the velocity course in time corresponded exactly to that given in the system in Equation (1) and presented in Figure 8.

The following values were assigned to the individual parameters: $V_{G,MAX} = 10 \text{ m/s}$, $T_0 = T_1 = T_3 = 0.4 \text{ s}$ and $T_2 = 0.8 \text{ s}$. A gust with such parameters caused a significant decrease in the angle of attack, which totaled $\alpha_{MIN} = -23.6^\circ$ (for a period of time of 0.8 s).

Figure 10 shows the obtained time courses of the drag, lift and pitching moment coefficients.

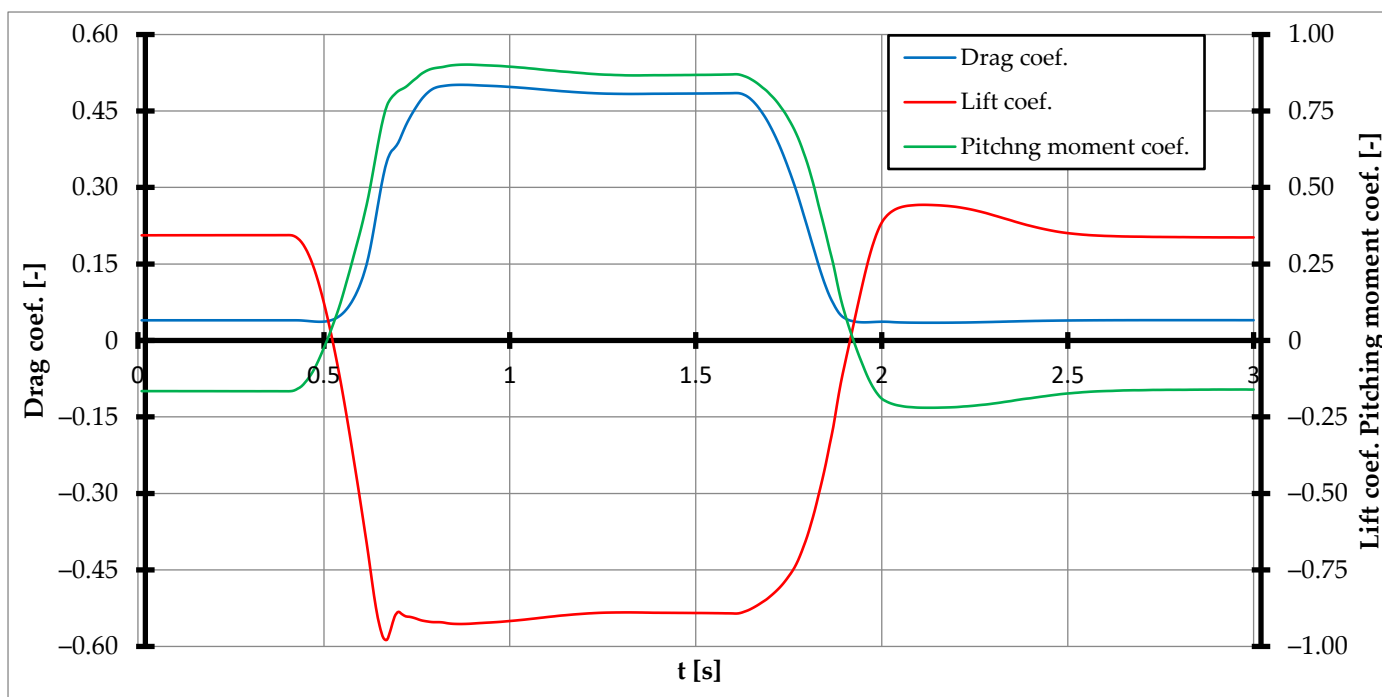


Figure 10. Time courses of UAV drag, lift and pitching moment coefficients under down draft.

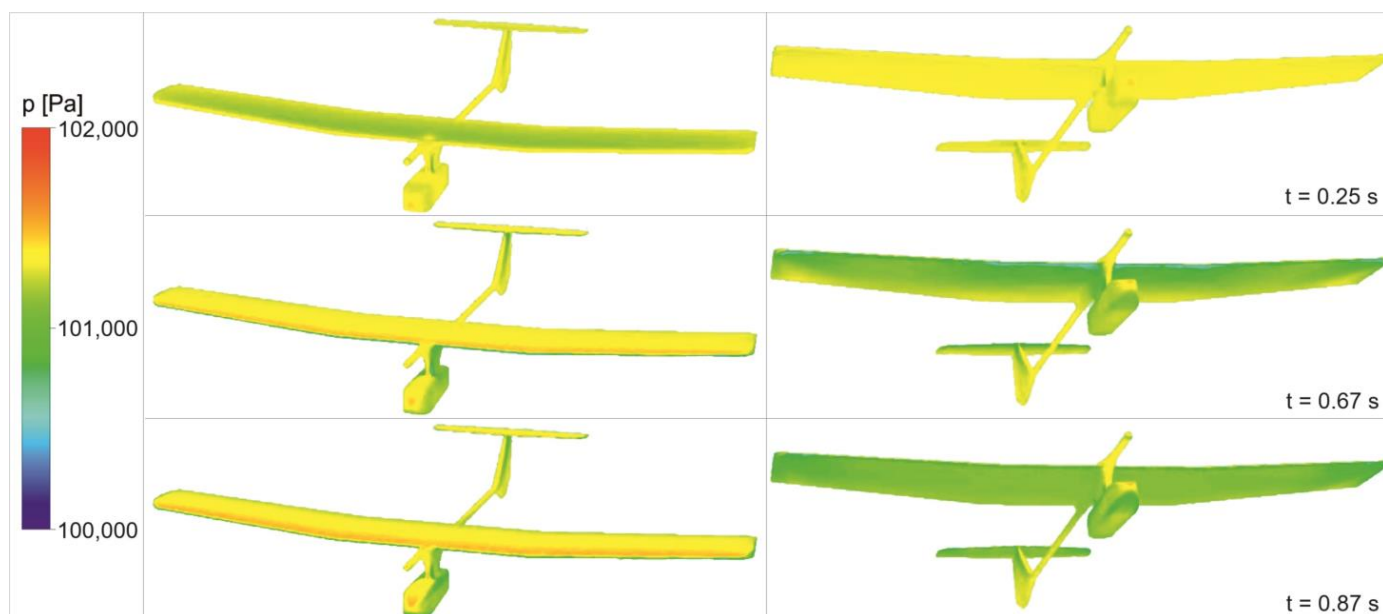
Additionally, obtained values of the aerodynamic coefficients with the corresponding time and angle of attack values are collected in Table 2 below.

It should be noted that the aerodynamic forces and pitching moment stabilized about 0.8 s after the gust ceased.

Figure 11 shows the contours of the pressure on the UAV surfaces corresponding to the conditions of the undisturbed flow (before the gust appeared), as well as corresponding to the maximal values of aerodynamic coefficients during the gust acting on the UAV.

Table 2. Aerodynamic coefficients for specific instants of time (downburst).

Time [s]	α [deg]	Drag Coef. [-]	Lift Coef. [-]	Pitching Moment Coef. [-]
0.4	2	0.039	0.344	-0.165
0.49	0	0.037 (local minimum)		
0.67	-16.4		-0.978 (minimum)	
0.7	-18.9		-0.887 (local maximum)	
0.87	-23.6	0.501 (maximum)	-0.927 (local minimum)	
0.89	-23.6			0.902 (maximum)
1.25 ÷ 1.6	23.6	0.483 ÷ 0.485	-0.892 ÷ 0.889	0.866 ÷ 0.87
2.11	2		0.433 (maximum)	
2.12	2	0.0035 (minimum)		
2.13	2			-0.22 (minimum)

**Figure 11.** Contours of static pressure on UAV surfaces before gust occurrence and for extremal values of aerodynamic forces and moment coefficients.

As it may be read from Figure 10 (as well as from Table 2), the extremal value of the lift coefficient occurred at $t = 0.67$ s (for $\alpha = -16.4^\circ$) and was equal to $C_{L,MIN} = 0.978$. The corresponding contour chart in Figure 11 shows that for $t = 0.67$ s there were regions of very low pressure (around 100,500 Pa) on the lower surface of the wings near the leading edges. Further increasing of the α value caused the airflow separation, which involved the whole lower surface of the wings. This separation is evident in Figure 11 (contours obtained for $t = 0.87$ s) and resulted in maximum value of the drag coefficient, which totaled $C_{D,MAX} = 0.501$. The airflow separation also caused the center of pressure displacement towards the wings trailing edge. Thus, the maximal value of the pitching moment coefficient was recorded at $t = 0.89$ s.

The transient aerodynamic characteristics described above are comparable to the steady-state stall analysis of airfoils [37]. However, for the downburst, the course of the lift coefficient vs. the angle of attack was prepared, as shown in Figure 12. The hysteresis loop in the presented chart is evident. Therefore, it is clear that the aerodynamic coefficients obtained during the stationary tests may differ significantly from actual ones under gust influence. As a consequence, gust occurrence during the flight of a UAV must be considered as a dynamic phenomenon.

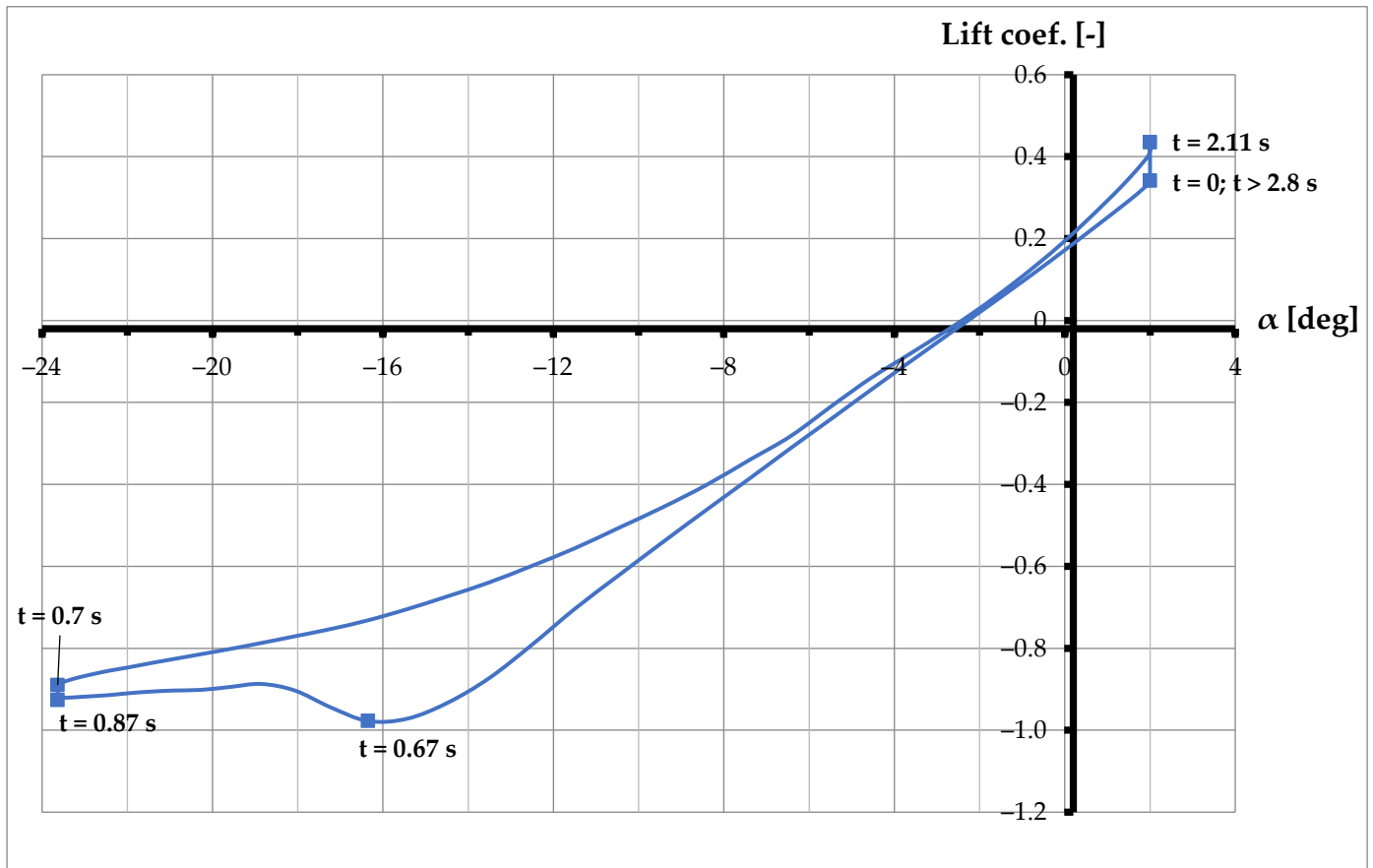


Figure 12. Lift coefficient as a function of the angle of attack during gust occurrence.

3.2.2. Oblique Gust

The second gust was characterized by the lifting and sliding angles, which equaled $\Theta_G = 45^\circ$ and $\Psi_G = 45^\circ$, respectively. The time course of the velocity is presented in Figure 13 and the corresponding function had following form:

$$\begin{cases} V_G = 0, & \text{for } t < T_0 \\ V_G = 0.5 \times V_{G,MAX} \times \left[1 - \cos\left(\pi \times \frac{t-T_0}{T_1}\right) \right], & \text{for } T_0 \leq t < T_0 + T_1 \\ V_G = V_{G,MAX} \times \left[0.9 + 0.1 \times \cos\left(\pi \times \frac{t-T_0-T_1}{T_2}\right) \right], & \text{for } T_0 + T_1 \leq t < T_0 + T_1 + T_2 \\ V_G = 0.5 \times V_{G,MAX} \times \left[1 + \cos\left(\pi \times \frac{t-T_0-T_1-T_2}{T_3}\right) \right], & \text{for } T_0 + T_1 + T_2 \leq t < T_0 + T_1 + T_2 + T_3 \\ V_G = 0, & \text{for } t \geq T_0 + T_1 + T_2 + T_3 \end{cases} \quad (9)$$

The following values from the function $V_G = f(t)$ were assumed: $V_{G,MAX} = 11.11$ m/s, $T_0 = T_1 = T_3 = 0.5$ s and $T_2 = 0.6$ s. A gust that presented such parameters caused the instantaneous angle of attack to reach values equal to $\alpha_{MAX} = 18.6^\circ$, and the angle of sideslip was $\beta_{MAX} = -11.4^\circ$.

Figure 14 presents the obtained courses of the aerodynamic force coefficients as a function of time, whereas the courses of the moment coefficients are shown in Figure 15.

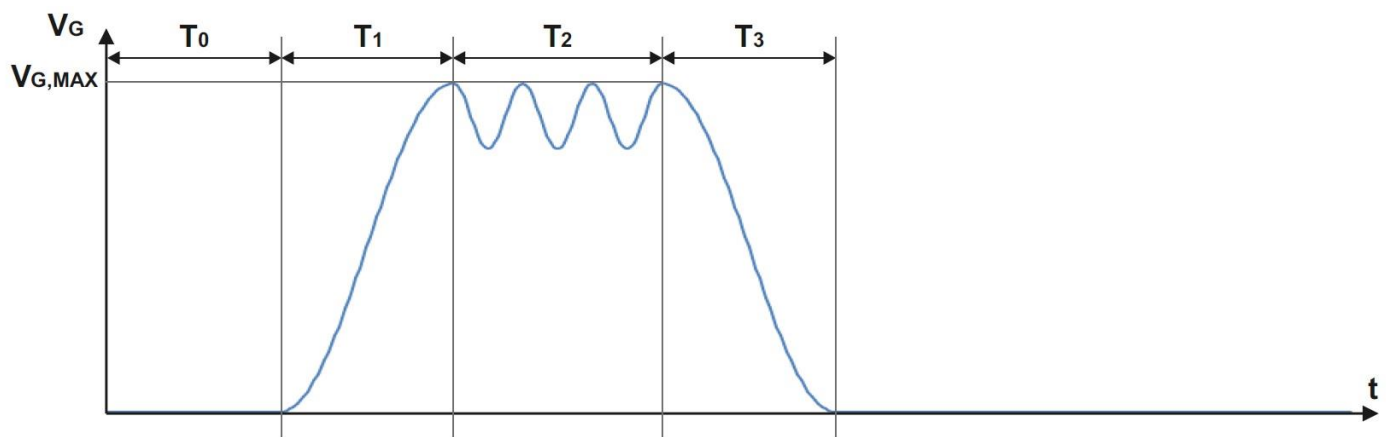


Figure 13. Time course of the oblique gust velocity magnitude.

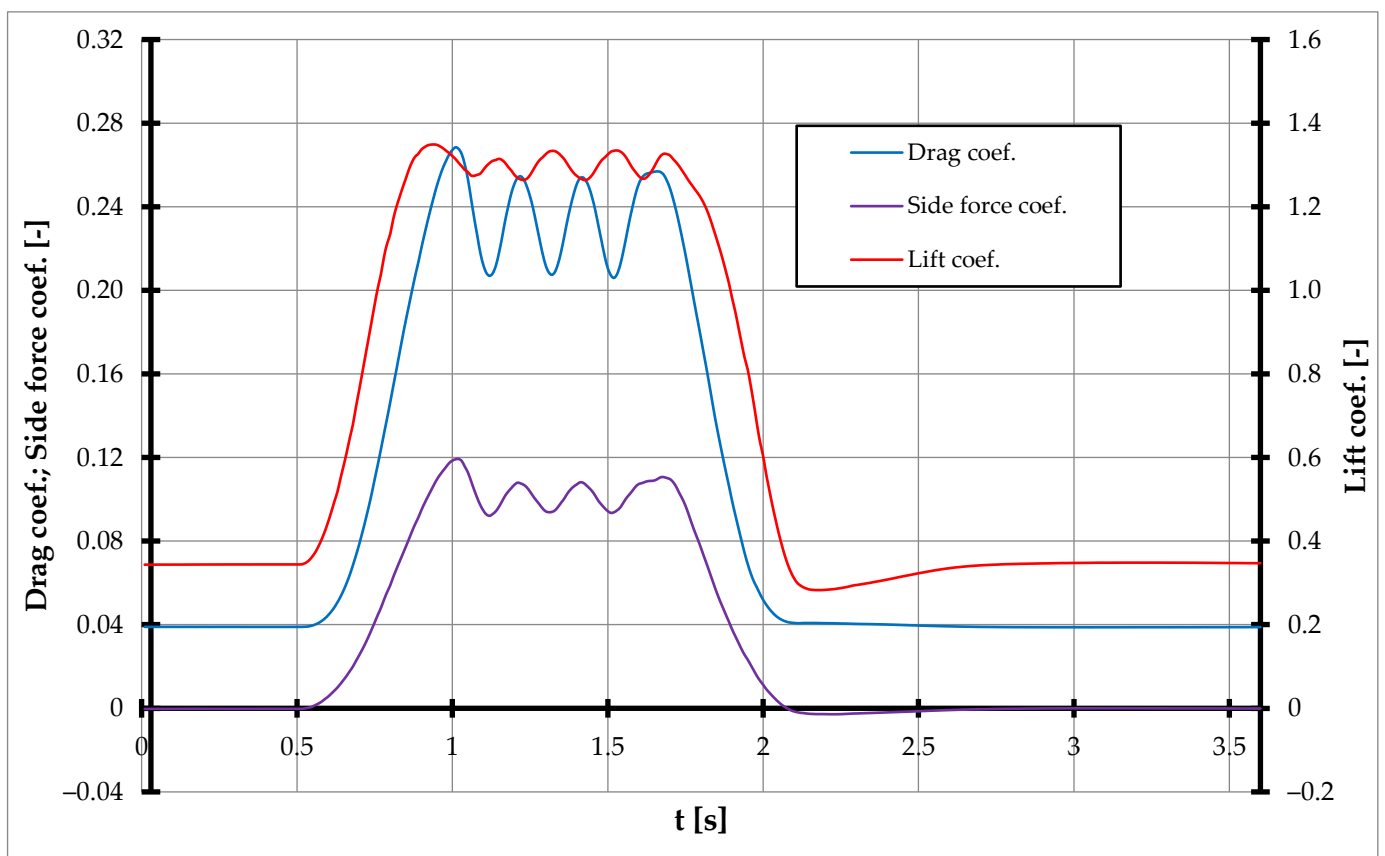


Figure 14. Time courses of UAV aerodynamic forces coefficients under an oblique gust.

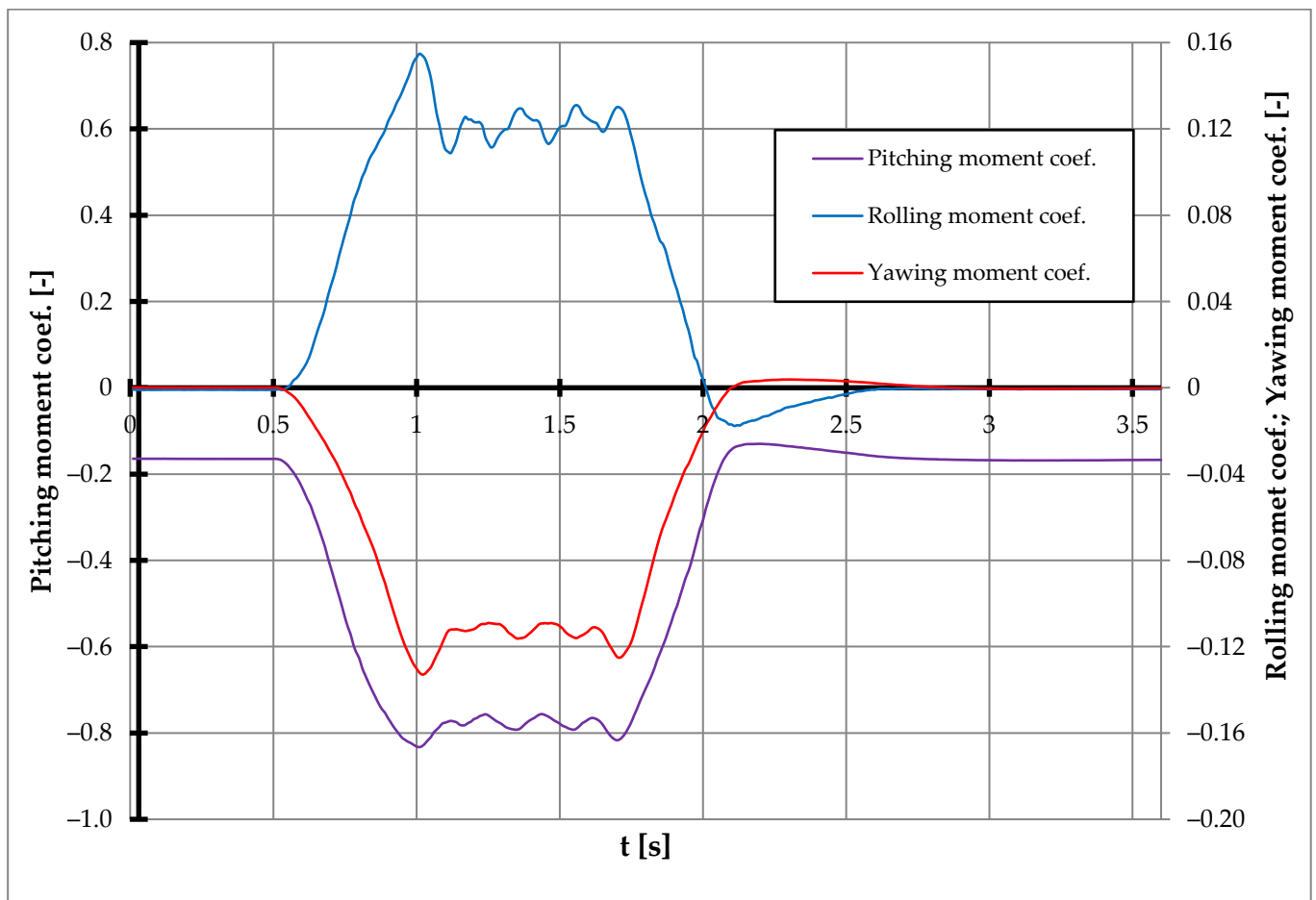


Figure 15. Time courses of UAV aerodynamic moment coefficients under an oblique gust.

The obtained values of the extremal aerodynamic coefficients with the corresponding time, angle of attack and angle of sideslip values are collected in Table 3 below.

Table 3. Extremal aerodynamic coefficients obtained for an oblique gust.

Time [s]	α [deg]	β [deg]	Drag Coef. [-]	Side Force Coef. [-]	Lift Coef. [-]	Rolling Moment Coef. [-]	Pitching Moment Coef. [-]	Yawing Moment Coef. [-]
0 ÷ 0.5	2	0	0.039	ca. 0	0.344	ca. 0	-0.165	ca. 0
0.94	17.8	10.9			1.35 max			
1.01	18.6	11.4	0.268 max			0.155 max	-0.833 min	
1.02	18.6	11.4		0.119 max				-0.133 min
2.11	2.02	0.02				-0.018 min		
2.18	2	0			0.283 min			
2.19	2	0					-0.13 max	
2.22	2	0		-0.003 min				
2.3	2	0						0.004 max
3.05	2	0	0.0388 min					

The aerodynamic coefficients returned to their state before the gust appeared (and stabilized) at the time of $t = 3$ s, i.e., after 0.9 s from the cessation of the gust, which is comparable to a downburst case.

Figure 16 shows the pressure contours on the UAV surfaces corresponding to the conditions of the undisturbed flow (before the gust appeared), as well as corresponding to the maximal values of the aerodynamic coefficients during the gust acting on the UAV.

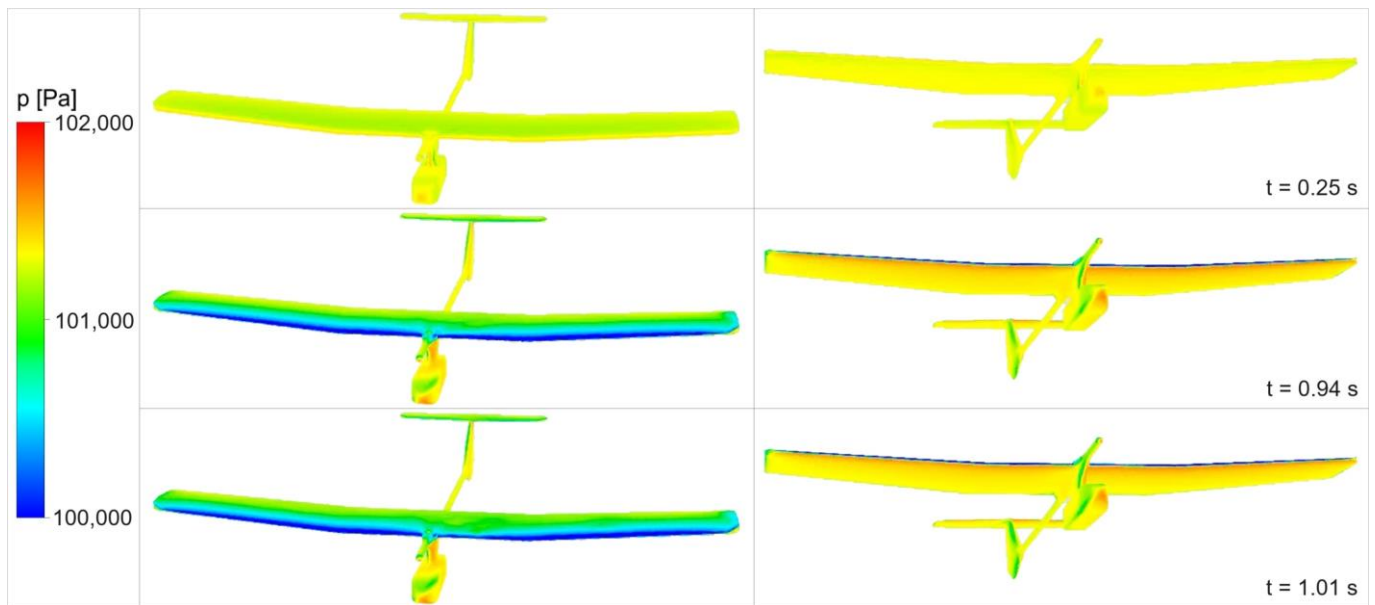


Figure 16. Contours of static pressure on UAV surfaces before gust occurrence and for extremal values of aerodynamic forces and moment coefficients.

As observed previously for the downburst case, the extremal value of the lift coefficient appeared prior to the extremal values of all the other aerodynamic coefficients. Figure 14 and Table 3 shows that it totaled $C_{L,MAX} = 1.35$ and occurred at $t = 0.94$ for $\alpha = 17.8^\circ$. Although the steady-state solution was performed for a symmetrical airflow, it should be highlighted that the maximum C_L obtained during the stationary numerical calculations was equal to 1.06 and was registered for $\alpha = 14^\circ$ (refer to Figure 9). The difference is significant. A possible explanation is that for the transient case, the full airflow separation occurred later (i.e., for a higher value of α), which was caused by the rapid increase of the α value under the gust influence. Figure 16 shows that at $t = 0.94$ s the region of low pressure (below 100,000 Pa) near the wing leading edge was widespread and quite uniform.

It was also observed that during the fluctuation in the gust velocity magnitude (which occurred in the time interval $t = [1 \text{ s}; 1.6 \text{ s}]$), repeated changes in the aerodynamic coefficients were noticed. It can be read from Figures 14 and 15 that the most irregular time course was that of the rolling moment coefficient. This can be explained by the nonhomogeneous flow separation from the wings' surface. The separation occurred together with unsymmetrical vortices. The total aerodynamic load on the wings changed over time in a repetitive manner (hence, the repetitive fluctuations in the aerodynamic forces coefficients). However, the variability of the load distribution resulted in an irregular character in the rolling moment time course. In Figure 16, the most unsymmetrical pressure contours may be observed for $t = 1.01$ s, which corresponded with the maximum value of the rolling moment coefficient.

It should be noted that the abovementioned rolling moment oscillations at high angles of attack are consistent with real-life experience, as airplanes that have stalled often tend to roll towards one of their wings.

4. Conclusions

This article presents the method of gust simulation using state-of-the-art CFD software (i.e., ANSYS Fluent Release 16.2), as well as the results from the research on the impact of gusts on UAV aerodynamic characteristics. Considering the universality of the presented method, surely it could be adopted to assess the vulnerability to gusts in wide selection of objects, including wind turbines.

An algorithm for determining the time-varying flow parameters on the boundary surfaces of the calculation domain was proposed. This algorithm involves the ANSYS Fluent UDF formulation for obtaining the variable in time–flow parameters, i.e., the velocity

magnitude and direction. The introduced method allows gusts of any speed course in time and in any direction to be modelled. Although it was not investigated in this study, the use of UDFs incorporating the presented flight mechanics formulas may be employed to model the gust with a time-varying direction.

Two gusts with maximal velocity magnitudes of 10 m/s and 11.1 m/s were simulated. Such events resulted in severe changes in the aerodynamic forces and moments of a UAV. For example, a downburst resulted in a negative lift (the value of C_L changed from 0.344 to minimal -0.978), whereas an oblique gust caused a change in the C_L from 0.344 to a maximal 1.35 (which was a 3.92-fold increase).

For each gust it was proved that the aerodynamic coefficients obtained during the stationary tests may differ substantially from the actual ones under gust influence. Moreover, based on the rolling moment time course, as well as on the contours of pressure on the UAV surfaces, it was observed that a rapid and significant angle of attack increase created a variable in time and nonhomogeneous separation on the wings.

As gust-induced changes in the aerodynamic coefficients may differ substantially from the ones obtained during stationary tests, the study is of great significance. For instance, the presented method can be utilized to obtain real gust-induced aerodynamic loads. Such research may also be exploited to modify autopilot algorithms used in this type of aircraft.

It should be noted that UAVs are increasingly used to perform autonomous flights and they can be highly exposed to gusts. Therefore, attempts to increase a UAV's resistance to gusts should be made. A lack of sufficient resistance may result in the falling of an object from the sky, causing threat to people on the ground, as well as loss of expensive payload or onboard equipment.

As mentioned, although the method of gust simulation was demonstrated on the basis of a UAV flight, it could also be utilized to assess the influence of gusts on a variety of objects. The impact of a turbulent atmosphere on wind turbine operation safety and performance seem to be important problems, as shown in numerous publications. Some of the presented methods could be implemented in subsequent studies focused on this subject area.

Author Contributions: Conceptualization, W.M., S.K. and M.F.; methodology, W.M. and M.F.; investigation, W.M. and M.F.; data curation, W.M.; validation, M.F.; writing—original draft preparation, W.M.; writing—review and editing, S.K.; supervision, S.K. All authors have read and agreed to the published version of the manuscript.

Funding: This research was funded by Military University of Technology, grant number UGB 820/2023.

Data Availability Statement: Not applicable.

Conflicts of Interest: The authors declare no conflict of interest.

References

1. Bowen, Y.; Pakwai, C.; Qiusheng, L.; Yuncheng, H.; Ying, C.; Zhenru, S.; Yao, C. Characterization of Wind Gusts: A Study Based on Meteorological Tower Observations. *Appl. Sci.* **2022**, *12*, 2105. [CrossRef]
2. Szwed, P.; Rzucidło, P.; Rogalski, T. Estimation of Atmospheric Gusts Using Integrated On-Board Systems of a Jet Transport Airplane—Flight Simulations. *Appl. Sci.* **2022**, *12*, 6349. [CrossRef]
3. Shelekhov, A.; Afanasiev, A.; Shelekhova, E.; Kobzev, A.; Tel'minov, A.; Molchunov, A.; Poplevina, O. High-Resolution Profiling of Atmospheric Turbulence Using UAV Autopilot Data. *Drones* **2023**, *7*, 412. [CrossRef]
4. Li, C.; Tan, H.; Wang, G.; Chan, P.; Luo, Y. Application of a Three-Dimensional Wind Field from a Phased-Array Weather Radar Network in Severe Convection Weather. *Atmosphere* **2023**, *14*, 781. [CrossRef]
5. Zhang, A.; Zhang, S.; Xu, X.; Zhong, H.; Li, B. Variation Characteristics of the Wind Field in a Typical Thunderstorm Event in Beijing. *Appl. Sci.* **2022**, *12*, 12036. [CrossRef]
6. Mohamed, A.; Marino, M.; Watkins, S.; Jaworski, J.; Jones, A. Gusts Encountered by Flying Vehicles in Proximity to Buildings. *Drones* **2023**, *7*, 22. [CrossRef]
7. *Aircraft Accident Report NTSB/AAR-86/05*; NTSB: Washington, DC, USA, 1986. Available online: <https://www.nts.gov/investigations/AccidentReports/Reports/AAR8605.pdf> (accessed on 25 August 2023).
8. *Weather-Related Aviation Accident Study 2003–2007*; FAA: Washington, DC, USA, 2010. Available online: <https://www.asias.faa.gov/i/studies/2003-2007weatherrelatedaviationaccidentstudy.pdf> (accessed on 25 August 2023).

9. Maślanka, P.; Szafrńska, H.; Aleksieiev, A.; Korycki, R.; Kaziur, P.; Dąbrowska, A. Influence of Material Degradation on Deformation of Paraglider during Flight. *Materials* **2023**, *16*, 5396. [[CrossRef](#)]
10. Chodnicki, M.; Siemiakowska, B.; Stecz, W.; Stępień, S. Energy Efficient UAV Flight Control Method in an Environment with Obstacles and Gusts of Wind. *Energies* **2022**, *15*, 3730. [[CrossRef](#)]
11. Jung, C.; Schindler, D.; Buchholz, A.; Liable, J. Global Gust Climate Evaluation and Its Influence on Wind Turbines. *Energies* **2017**, *10*, 1474. [[CrossRef](#)]
12. Chiodo, E.; Diban, B.; Mazzanti, G.; De Angelis, F. A Review on Wind Speed Extreme Values Modeling and Bayes Estimation for Wind Power Plant Design and Construction. *Energies* **2023**, *16*, 5456. [[CrossRef](#)]
13. Herisanu, N.; Marinca, V.; Madescu, G.; Dragan, F. Dynamic Response of a Permanent Magnet Synchronous Generator to a Wind Gust. *Energies* **2019**, *12*, 915. [[CrossRef](#)]
14. Yitao, Z.; Zhigang, W.; Chao, Y. Study of Gust Calculation and Gust Alleviation: Simulations and Wind Tunnel Tests. *Aerospace* **2023**, *10*, 139. [[CrossRef](#)]
15. Reischich, A.; Finster, M.; Heinrich, M.; Schwarze, R. Effect of Flexible Flaps on Lift and Drag of Laminar Profile Flow. *Energies* **2020**, *13*, 1077. [[CrossRef](#)]
16. Kotsiopoulou, M.; Bouris, D. Numerical Simulation of the Effect of a Single Gust on the Flow Past a Square Cylinder. *Fluids* **2022**, *7*, 303. [[CrossRef](#)]
17. Lakshmi, S.; Nishanth, R.; Sudharshan, B.R.; Unnikrishnan, D.; Akram, M.; Ratna, K.V. Effect of Macroscopic Turbulent Gust on the Aerodynamic Performance of Vertical Axis Wind Turbine. *Energies* **2023**, *16*, 2250. [[CrossRef](#)]
18. Santo, G.; Peeters, M.; Van Paepegem, W.; Degroote, J. Fluid–Structure Interaction Simulations of a Wind Gust Impacting on the Blades of a Large Horizontal Axis Wind Turbine. *Energies* **2020**, *13*, 509. [[CrossRef](#)]
19. Cai, X.; Pan, P.; Zhu, J.; Gu, R. The Analysis of the Aerodynamic Character and Structural Response of Large-Scale Wind Turbine Blades. *Energies* **2013**, *6*, 3134–3148. [[CrossRef](#)]
20. Benaouali, A.; Kachel, S. Multidisciplinary Design Optimization of Aircraft Wing Using Commercial Software Integration. *Aerosp. Sci. Technol.* **2019**, *92*, 766–776. [[CrossRef](#)]
21. Kozakiewicz, A.; Frant, M.; Majcher, M. Impact of the Intake Vortex on the Stability of the Turbine Jet Engine Intake System. *Int. Rev. Aerosp. Eng.* **2021**, *14*, 173. [[CrossRef](#)]
22. Wu, C.-H.; Chen, J.-Z.; Lo, Y.-L.; Fu, C.-L. Numerical and Experimental Studies on the Aerodynamics of NACA64 and DU40 Airfoils at Low Reynolds Numbers. *Appl. Sci.* **2023**, *13*, 1478. [[CrossRef](#)]
23. Frant, M. Numerical Analysis of Complex Objects Aerodynamics Using Finite Volume Methods. Ph.D. Thesis, Military University of Technology, Warsaw, Poland, 2010.
24. Cravero, C.; De Domenico, D.; Marsano, D. The Use of Uncertainty Quantification and Numerical Optimization to Support the Design and Operation Management of Air-Staging Gas Recirculation Strategies in Glass Furnaces. *Fluids* **2023**, *8*, 76. [[CrossRef](#)]
25. Xia, L.; Zou, Z.J.; Wang, Z.H.; Zou, L.; Gao, H. Surrogate model based uncertainty quantification of CFD simulations of the viscous flow around a ship advancing in shallow water. *Ocean Eng.* **2021**, *234*, 109206. [[CrossRef](#)]
26. Cravero, C.; De Domenico, D.; Marsano, D. Uncertainty Quantification Analysis of Exhaust Gas Plume in a Crosswind. *Energies* **2023**, *16*, 3549. [[CrossRef](#)]
27. Huang, Y.; Guo, X.; Cao, D. Aerodynamic Characteristics of a Z-Shaped Folding Wing. *Aerospace* **2023**, *10*, 749. [[CrossRef](#)]
28. Tofan-Negru, A.; Ștefan, A.; Grigore, L.S.; Oncioiu, I. Experimental and Numerical Considerations for the Motor-Propeller Assembly's Air Flow Field over a Quadcopter's Arm. *Drones* **2023**, *7*, 199. [[CrossRef](#)]
29. Zhang, Z.; Xie, C.; Wang, W.; An, C. An Experimental and Numerical Evaluation of the Aerodynamic Performance of a UAV Propeller Considering Pitch Motion. *Drones* **2023**, *7*, 447. [[CrossRef](#)]
30. Ghirardelli, M.; Kral, S.; Müller, N.; Hann, R.; Cheynet, E.; Reuder, J. Flow Structure around a Multicopter Drone: A Computational Fluid Dynamics Analysis for Sensor Placement Considerations. *Drones* **2023**, *7*, 467. [[CrossRef](#)]
31. Pérez Gordillo, A.M.; Escobar, J.A.; Lopez Mejia, O.D. Influence of the Reynolds Number on the Aerodynamic Performance of a Small Rotor. *Aerospace* **2023**, *10*, 130. [[CrossRef](#)]
32. Lei, Y.; Li, Y.; Wang, J. Aerodynamic Analysis of an Orthogonal Octorotor UAV Considering Horizontal Wind Disturbance. *Aerospace* **2023**, *10*, 525. [[CrossRef](#)]
33. *ANSYS FLUENT Theory Guide*; ANSYS, Inc.: Canonsburg, PA, USA, 2015.
34. Krzyżanowski, A. *Mechanika Lotu*; Wydźiał Wydawniczy WAT: Warsaw, Poland, 2009.
35. *ANSYS FLUENT UDF Manual*; ANSYS, Inc.: Canonsburg, PA, USA, 2015.
36. Yousefi, K.; Razeghi, A. Determination of the Critical Reynolds Number for Flow over Symmetric NACA Airfoils. In Proceedings of the 2018 AIAA Aerospace Sciences Meeting, Kissimmee, FL, USA, 8–12 January 2018. [[CrossRef](#)]
37. Skrzypinski, W.; Zahle, F.; Bak, C. Parametric approximation of airfoil aerodynamic coefficients at high angles of attack. In Proceedings of the European Wind Energy Conference & Exhibition 2014, Barcelona, Spain, 10–13 March 2014; Available online: https://backend.orbit.dtu.dk/ws/files/89913457/Parametric_approximation_of_airfoil.pdf (accessed on 25 August 2023).

Disclaimer/Publisher's Note: The statements, opinions and data contained in all publications are solely those of the individual author(s) and contributor(s) and not of MDPI and/or the editor(s). MDPI and/or the editor(s) disclaim responsibility for any injury to people or property resulting from any ideas, methods, instructions or products referred to in the content.